

# Microstructural Evolution of Secondary Phases in the Cast Duplex Stainless Steels CD3MN and CD3MWCuN

YOON-JUN KIM, OZAN UGURLU, CHAO JIANG, BRIAN GLEESON,  
and L. SCOTT CHUMBLEY

The isothermal formation behavior of secondary phases in two types of duplex stainless steels (DSS), CD3MN and CD3MWCuN, was characterized. Samples were heat treated from 1 minute to 30 days at temperatures from 700 °C to 900 °C. Small carbide ( $M_{23}C_6$ ) and nitride ( $Cr_2N$ ) precipitates, together with the intermetallic phases sigma and chi, were observed using scanning electron microscopy (SEM) and confirmed by transmission electron microscopy (TEM) analyses. Based on SEM analysis, time-temperature-transformation (TTT) curves for the sigma and chi phases were determined by measuring their volume fractions from backscattered electron micrographs of heat-treated and quenched sample cross sections. Resulting TTT curves showed that the maximum formation temperature for chi is lower than that for sigma, while the time to reach 1 vol pct formation is much less for sigma than it is for chi. The thermodynamic driving forces associated with the sigma and chi formation were assessed using Thermo-Calc.

DOI: 10.1007/s11661-006-9049-6

© The Minerals, Metals & Materials Society and ASM International 2007

## I. INTRODUCTION

DUPLEX stainless steels (DSS) possessing both ferrite ( $\delta$ ) and austenite ( $\gamma$ ) as primary phases are produced by adding Cr, Mo, Si, Ni, Mn, and N to a base Fe-C system. The addition of such alloying elements affects the relative stability of existing phases and also causes new phases to form. Elements such as Cr, Si, and Mo are called ferrite stabilizers because they promote ferrite phase formation over wider composition and temperature ranges as compared to the Fe-C system. Concurrently, the austenite region is contracted, *i.e.*, the  $\gamma$  loop shrinks. By contrast, elements such as C, Ni, Mn, and N promote austenite formation and are called austenite stabilizers. Both ferrite and austenite co-exist in DSS by adjusting the ratio of ferrite-to-austenite stabilizers. The two-phase microstructure of such steels confers a favorable combination of mechanical and corrosion properties.

Because DSS are highly alloyed, many secondary phases other than  $\delta$  and  $\gamma$  may also form during either service or fabrication. Typical secondary phases that have been reported<sup>[1]</sup> are listed in Table I and include secondary austenite ( $\gamma_2$ ), carbides such as  $M_7C_3$  and  $M_{23}C_6$ , and various types of intermetallic phases such as  $\sigma$ ,  $\chi$ , R, and  $\pi$ . Secondary austenite ( $\gamma_2$ ) has the same crystal structure as primary austenite ( $\gamma_1$ ); however, the lattice parameter and the formation temperature are slightly different from the primary form. In spite of their differences, the physical and mechanical properties of  $\gamma$

and  $\gamma_2$  are quite similar.<sup>[1]</sup> Austenite is known to improve mechanical properties such as fracture toughness<sup>[1]</sup> and is beneficial to DSS performance. The carbon content in DSS is usually very low (less than 0.03 wt pct), and, as a consequence, the amount of carbide is typically too low to significantly affect the mechanical properties. The carbides usually form in conjunction with  $\gamma_2$  and  $\sigma$ <sup>[2]</sup> to result in dual-phase morphologies. The formation mechanism of nitrides such as  $Cr_2N$  in DSS has also been reported.<sup>[3]</sup>

The phases most deleterious to mechanical and corrosion properties of DSS are the Cr- and Mo-rich intermetallics, because they are brittle and reduce the steel's resistance to pitting corrosion due to depletion of Cr and Mo from the  $\delta$  matrix.<sup>[1,4,5,14]</sup> The Cr-rich  $\sigma$  phase has a tetragonal lattice structure and its nucleation is usually observed at the interphase boundary between  $\delta$  and  $\gamma$ .<sup>[1-12]</sup> The Mo-rich  $\chi$  phase has a cubic crystal structure and its formation may be detrimental to the impact toughness of DSS.<sup>[15,16]</sup> The  $\chi$  phase is reported to be more brittle than  $\sigma$ .<sup>[4]</sup>

Time-temperature-transformation (TTT) and continuous-cooling-transformation diagrams are useful for assessing the transformation behavior and stability of detrimental intermetallic phases in DSS. Accordingly, several transformation assessment studies have been conducted on various wrought alloys.<sup>[6-11]</sup> Recent studies by the present authors<sup>[12,13]</sup> on CD3MN and CD3MWCuN represent the only known work on the phase transformation kinetics of cast DSS. These recent studies employed optical microscopy and tint etching to examine phase precipitation and to determine the extent of transformation. However, the tint-etched colors of both  $\sigma$  and  $\chi$  are too similar to allow for an unambiguous identification. Thus, the initial diagrams developed contained collective initial and final intermetallic forma-

Y.-J. KIM, Research Engineer, is with the Hyundai-Kia Motors, Seoul, South Korea. O. UGURLU and C. JIANG, Research Scientists, are with the Los Alamos National Laboratory, Los Alamos, NM, USA. B. GLEESON and L. SCOTT CHUMBLEY, Professors, are with the Ames Laboratory, Iowa State University, IA 50011, USA. Contact e-mail: chumbley@iastate.edu

Manuscript submitted August 11, 2006.

**Table I. Common Secondary Phases in DSS<sup>11</sup>**

Phase	Lattice Type (Structure Type)	Space Group (Pearson Symbol)	Lattice Parameter, Å	Formation Temperature, °C
$\delta$	bcc (W)	<i>Im m</i> ( <i>cI2</i> )	$a = 2.86$ to $2.88$	All temperatures
$\gamma/\gamma_2$	fcc (Cu)	<i>Fm m</i> ( <i>cF4</i> )	$a = 3.58$ to $3.62$	700 to 900 ( $\gamma_2$ )
$\sigma$	tetragonal (CrFe)	<i>P4<sub>2</sub>/mmm</i> ( <i>tP30</i> )	$a = 8.79$ , $c = 4.54$	600 to 1000
$\chi$	cubic (Mn)	<i>I 3m</i> ( <i>cI58</i> )	$a = 8.92$	700 to 900
R	rhombohedral (Mo)	<i>R3</i> ( <i>hR53</i> )	$a = 10.90$ , $c = 19.34$	550 to 800
$\pi$	cubic (Mn)	<i>P4<sub>1</sub>32</i> ( <i>cP20</i> )	$a = 6.47$	≈600
Cr <sub>2</sub> N	hexagonal (Fe <sub>2</sub> N)	<i>P 1m</i> ( <i>hP9</i> )	$a = 4.80$ , $c = 4.47$	700 to 900
M <sub>23</sub> C <sub>6</sub>	cubic (C <sub>6</sub> Cr <sub>23</sub> )	<i>Fm m</i> ( <i>cF116</i> )	$a = 10.56$ to $10.65$	< 950
M <sub>7</sub> C <sub>3</sub>	orthorhombic (C <sub>3</sub> Cr <sub>7</sub> )	<i>Pnma</i> ( <i>oP20</i> )	$a = 4.52$ , $b = 6.99$ , $c = 12.11$	950 to 1050

tion curves, rather than separate curves for  $\sigma$  and  $\chi$ . A further phase characterization study was therefore undertaken using detailed scanning electron microscopy (SEM) and transmission electron microscopy (TEM), coupled with compositional analysis using energy-dispersive spectroscopy (EDS). Based upon the various characterizing methods used, the aim of this study was to clarify the phase identification of secondary phases formed in DSS alloys, thus producing more accurate transformation curves.

## II. EXPERIMENTAL PROCEDURES

Cast DSS, CD3MN (alternatively, UNS J92205 or ASTM A 890/A 890M 99 Grade 4A) and CD3MWCuN (alternatively, UNS J93380 or ASTM A 890/A 890M 99 Grade 6A), were received in the form of keel bars of approximate size  $3 \times 4 \times 35$  cm. The primary designations used for these steels are in accordance with the Alloy Casting Institute. The measured composition, heat treatment, metallography, and quantitative measurement methods used are described in detail elsewhere.<sup>[12]</sup> Briefly, small coupons about 4 mm in thickness were sliced from the blocks by electric discharge machining. The coupons were first heated at 1100 °C for 30 minutes in order to achieve an initial  $\gamma/\delta$  ratio of 50:50, and then quickly cooled to an isothermal annealing temperature in the range of 750 °C to 900 °C and held in a salt bath or a box furnace for times ranging from 1 minute to 1 month. At the end of a given anneal, the coupons were quenched in water. Cross sections of the coupons were prepared using standard metallographic techniques. Each sample was electrolytically etched in a 50 g NaOH + 100 mL H<sub>2</sub>O solution for approximately 10 seconds at 6 V. The area fraction of intermetallic  $\sigma$  and  $\chi$  phases was measured using a scanning electron microscope equipped with an image analysis system and operated in the backscattered electron imaging mode. The SEM images were taken at 1000 times magnification.

Phase identification was carried out on selected samples using a Philips\* CM30 transmission electron microscope

at 300 KeV. A CD3MN sample heat treated at 850 °C for 30 days and a CD3MWCuN sample heat treated at 850 °C for 3 days were analyzed, because they were expected to contain the greatest number of possible phases. The TEM foils were prepared using the jet polishing method, in which the solution used was 5 pct perchloric acid + 25 pct glycerol + 70 pct ethanol at a temperature of -20 °C and a potential of 50 V. An energy dispersive spectrometer attached to a transmission electron microscope was used for initial screening of the possible phases and to quantify the compositions. A more accurate determination of phase composition was carried out on polished bulk samples using an electron probe microanalyzer equipped with wavelength dispersive spectrometers.

## III. EXPERIMENTAL AND CALCULATED RESULTS

### A. TEM Analysis

Identification of the precipitate phases in the heat-treated cast alloys was initially determined using EDS to locate potential regions in the sample for detailed electron diffraction analysis. Once a region was identified, a combination of selected area diffraction (SAD) and convergent beam electron diffraction was used, with the results being compared to the crystallographic information listed in Table I. In terms of microstructural evolution, the steels studied contained approximately a 50:50 ferrite-to-austenite ratio at the beginning of isothermal transformation. Secondary phases such as  $\gamma_2$ ,  $\sigma$ , and  $\chi$  started to form at  $\delta/\gamma$  interphase boundaries during the course of subsequent isothermal annealing. As will be shown in more detail in Section B, at long times, the  $\delta$  ferrite was consumed by the formation of intermetallic compounds.

The most commonly observed intermetallic precipitates in both steels were found to be  $\sigma$  and  $\chi$ . An example of a  $\sigma$  precipitate in the CD3MN steel is shown in Figure 1, which also includes a selected area diffraction pattern from the [100] zone axis. The  $\chi$  phase (Figure 2) was also observed but to a much lesser extent. Both the  $\chi$  and  $\sigma$  phases appeared large and relatively equiaxed, as might be expected if they were growing at the expense of an equiaxed  $\delta$  ferrite grain.

A number of small roughly circular precipitates were also found. Cr-rich precipitates, identified as

\*Philips is a trademark of Philips Electronic Instruments Corp., Mahwah, NJ.

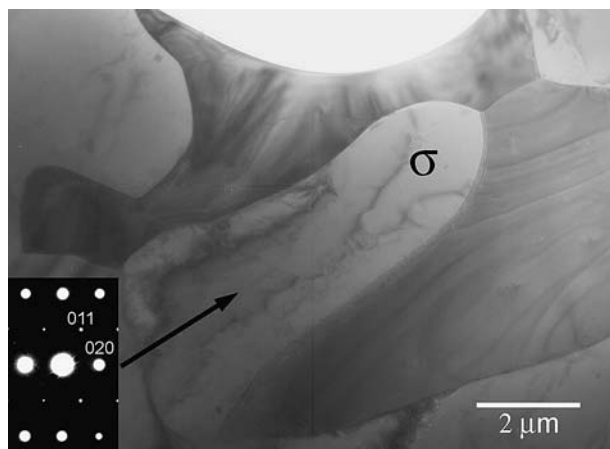


Fig. 1—Bright-field image of  $\sigma$  phase in CD3MN heat treated 30 days at 850 °C. The inset shows the [100] zone axis from the  $\sigma$ -phase grain.

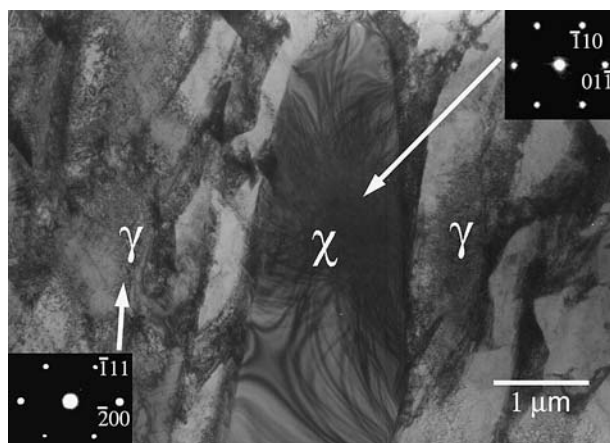


Fig. 2—Bright-field image of  $\gamma$  and  $\chi$  grains in CD3MN heat treated 30 days at 850 °C. The insets show the [011] SAD pattern obtained from the  $\gamma$  and [111] SAD pattern from  $\chi$ .

$M_{23}C_6$ -type carbide (Figure 3), were present throughout the CD3MN sample. These precipitates were usually observed at  $\gamma$  grain boundaries.  $Cr_2N$  precipitates were also easily identified in CD3MN (Figure 4). These latter precipitates usually occurred in small clusters or groups, often somewhat aligned. Both the carbides and nitrides were more difficult to find in the TEM samples of CD3MWCuN. Other types of secondary phases listed in Table I, such as  $M_7C_3$ ,  $R$ , and  $\pi$ , were not observed in the current investigation in either CD3MN or CD3MWCuN. Table II compares the lattice parameters calculated from diffraction patterns obtained in this study to those obtained from the references. The agreement seems to be quite good. The contents of the major elements, as determined semiquantitatively using EDS in TEM, are also listed in this table.

### B. SEM Analysis

Typical microstructures from CD3MN heat treated for 30 days at 850 °C and CD3MWCuN heat treated

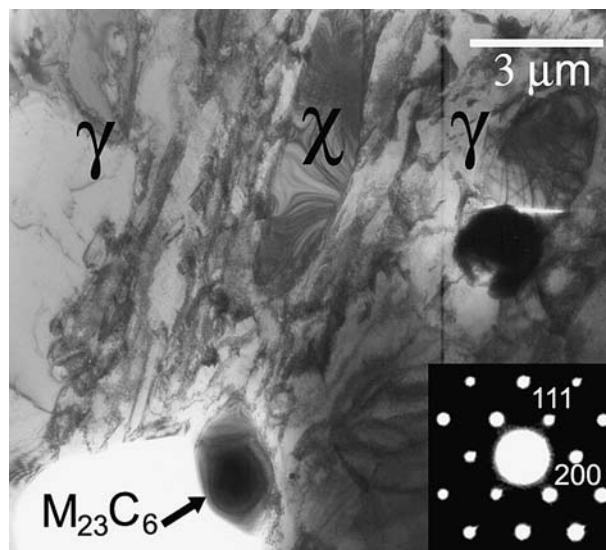


Fig. 3—Bright-field image of CD3MN heat treated 30 days at 850 °C. The SAD pattern (inset) shows the [011] zone axis from the indicated  $M_{23}C_6$  phase particle (arrowed).

for 3 days at the same temperature are shown in Figure 5(a) and (b), respectively. The contrast variation in these backscattered electron (BSE) images due to atomic number differences in the phases, coupled with EDS measurements, allowed for correlation with the TEM results. The matrix in both steels consisted predominantly of  $\gamma$  (gray), with only small amounts of  $\delta$  (dark gray) present. The  $M_{23}C_6$ -type carbides identified by TEM appeared as precipitates along globular-shaped  $\gamma$  boundaries. In agreement with the TEM analyses, fewer carbides were observed in the CD3MWCuN sample than in CD3MN. The  $\sigma$  phase appears light gray in Figure 5 and it is evident from the CD3MN image (Figure 5(a)) that  $\sigma$  growth involved the consumption of  $\delta$ . It is noted that the difficulty in

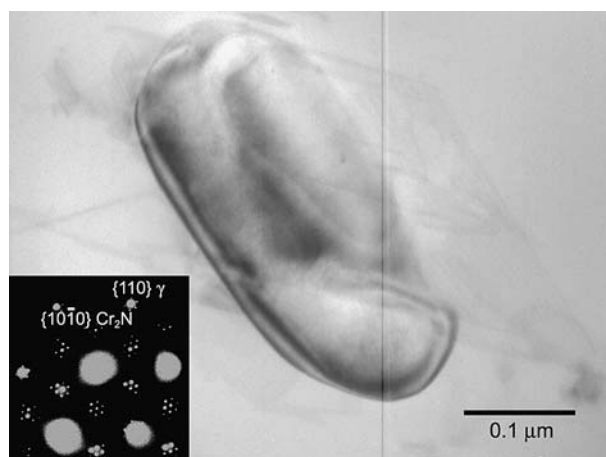


Fig. 4—Bright-field image of  $Cr_2N$  phase in CD3MN heat treated 30 days at 850 °C. The SAD pattern (inset) shows the  $Cr_2N$  [0001] zone axis aligned with the [111] zone axis of  $\gamma$ . Numerous extra reflections around the  $Cr_2N$   $\{10\bar{1}0\}$  are due to double diffraction effects.

**Table II. Calculated Lattice Parameters of Phases Identified**

Phases	Reference Lattice Parameter, Å	Experimental Lattice Parameter, Å	Composition Measured by EDS (Wt Pct)
$\gamma/\gamma_2$	$a = 3.58$ to $3.62$	$a \approx 3.61$	70Fe-21Cr-6.0Ni-1.5Mo
$\sigma$	$a = 8.79$ , $c = 4.54$	$a \approx 8.83$ , $c \approx 4.55$	56Fe-35Cr-4.5Ni-2.8Mo
$\chi$	$a = 8.92$	$a \approx 8.89$	51Fe-24Cr-2.1Ni-21Mo
$\text{Cr}_2\text{N}$	$a = 4.80$ , $c = 4.47$	$a \approx 4.70$ , $c \approx 4.47$	8.6Fe-88Cr-2.8Mo (N omitted)
$\text{M}_{23}\text{C}_6$	$a = 10.56$ to $10.65$	$a \approx 10.67$	21Fe-61Cr-1.2Ni-11Mo-5.0C

differentiating between  $\sigma$  and  $\chi$  in the optical images does not exist in BSE images. Both  $\sigma$  and  $\chi$  contain Fe, Cr, Mo, and Ni as major elements; however, as will be shown in Section C,  $\sigma$  is richer in Cr while  $\chi$  is richer in Mo. This causes the  $\chi$  phase to appear brighter than  $\sigma$  in BSE images.

A fine distribution of small white particles is also seen within the  $\gamma$  grains in Figure 5. These particles have the size, shape, and clustering observed for the  $\text{Cr}_2\text{N}$  particles in TEM. The relatively high Cr content, as measured by EDS in the TEM, causes these particles to also appear white when compared to the matrix. Fewer

$\text{Cr}_2\text{N}$  particles are visible in the CD3MWCuN sample than in CD3MN.

Investigation of the chemical compositions of the major phases using wavelength dispersive spectroscopy (WDS) involved samples annealed at short and long times to effectively represent the start of precipitation and the establishment of equilibrium conditions. Concentrations of the major alloying elements such as Fe, Cr, Mo, and Ni in the  $\delta$ ,  $\gamma$ ,  $\sigma$ , and  $\chi$  phases were found to vary slightly with annealing time, as might be expected in a diffusion-controlled process. Typical results for short and long annealing times are summarized in Tables III and IV, respectively. The composition of  $\sigma$  in CD3MN after 30 minutes annealing and  $\chi$  in CD3MWCuN after 10 minutes annealing could not be accurately measured using EDS in the SEM due to their small size. It is noted that the amount of  $\delta$  in CD3MWCuN after 3 days annealing was essentially zero. Further, in the short-time annealed samples (*i.e.*, 30 min for CD3MN and 10 min for CD3MWCuN), the amount of intermetallic phase present was so low it was difficult to discern between  $\chi$  and  $\sigma$  simply on the basis of contrast in the SEM, even when using BSE imaging. This is because, with only a single phase present, the contrast can be made to appear white or light gray simply by varying the SEM contrast and brightness controls.

### C. Thermodynamic Calculations

Parallel to experimental investigations, equilibrium thermodynamic calculations were also performed in the present study using the CALPHAD (calculation of phase diagrams) approach, as implemented in the Thermo-Calc software package.<sup>[18]</sup> The 850 °C equilibrium phase compositions for both CD3MN and CD3MWCuN alloys were calculated. The most recent iron and steel database, TCFE3, was used in these calculations. The calculation results are included in Tables III and IV and are seen to be in reasonable agreement with the experimental measurements. Further, the calculations clearly confirm that  $\chi$  is especially rich in Mo when compared to  $\sigma$  (about 16 to 18 wt pct vs 6 to 8 wt pct), while  $\sigma$  is slightly enriched in Cr compared to  $\chi$ . Therefore, the initial intermetallic phases that contained relatively high Mo are inferred to be  $\chi$ , while those particles that contained low Mo and high Cr are considered to be  $\sigma$ . According to such criteria, the intermetallic phase first formed after 30 minutes in CD3MN is believed to be  $\chi$ . Just the opposite is true for CD3MWCuN, where, on the basis of composition,  $\sigma$  appears to be the first to form.

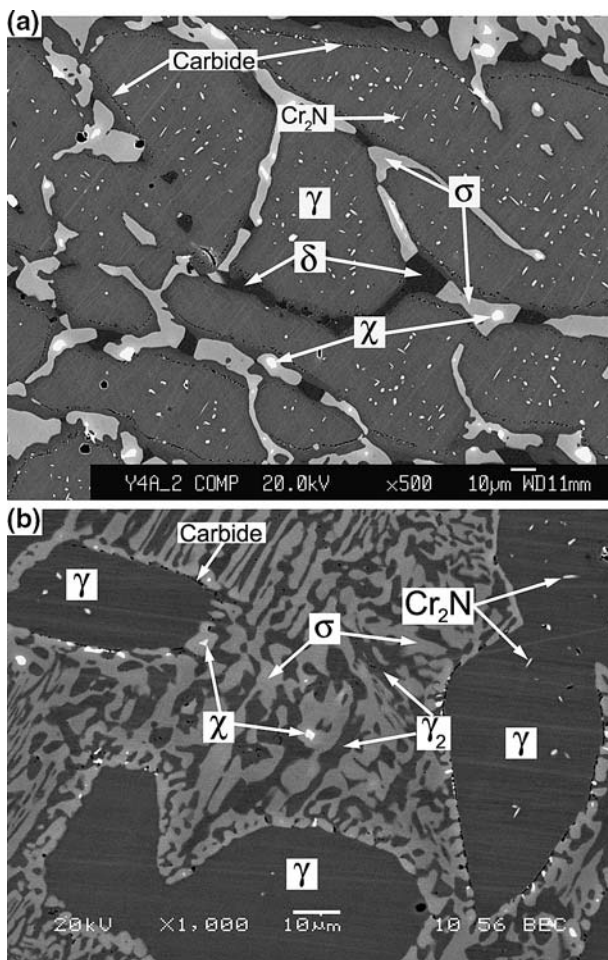


Fig. 5—BSE image of (a) CD3MN annealed for 30 days and (b) CD3MWCuN annealed for 3 days. The chi phase is brighter than sigma in the BSE image.

**Table III. Composition (Weight Percent) of CD3Mn Phases by WDS; the Equilibrium Phase Compositions Calculated by Thermo-Calc Using the TCFe3 Database are Shown in Parentheses**

Phases	Fe	Cr	Ni	Mo	Si	Mn	W	Cu
(a) CD3Mn Sample Annealed 30 Min at 850 °C								
$\delta$	64.58 $\pm$ 0.74	24.16 $\pm$ 0.33	4.08 $\pm$ 0.30	3.46 $\pm$ 0.078	0.66 $\pm$ 0.019	0.65 $\pm$ 0.041	0.058 $\pm$ 0.053	0.17 $\pm$ 0.024
$\gamma$	66.09 $\pm$ 0.70	21.11 $\pm$ 0.21	6.51 $\pm$ 0.090	2.18 $\pm$ 0.033	0.57 $\pm$ 0.027	0.74 $\pm$ 0.036	0.031 $\pm$ 0.035	0.22 $\pm$ 0.028
$\sigma$	No data obtained							
$\chi$	53.65 $\pm$ 0.34	25.62 $\pm$ 0.26	3.00 $\pm$ 0.098	14.35 $\pm$ 0.12	1.04 $\pm$ 0.014	0.70 $\pm$ 0.030	0.25 $\pm$ 0.004	0.045 $\pm$ 0.020
(b) CD3Mn Sample Annealed 30 Days at 850 °C								
$\delta$	67.93 $\pm$ 2.88 (67.84)	24.12 $\pm$ 1.63 (24.68)	2.23 $\pm$ 0.27 (3.10)	2.36 $\pm$ 1.37 (2.86)	0.68 $\pm$ 0.10 (0.81)	0.39 $\pm$ 0.045 (0.57)	0.027 $\pm$ 0.025 (0)	0.093 $\pm$ 0.032 (0.14)
$\gamma$	67.12 $\pm$ 1.30 (71.10)	20.44 $\pm$ 1.00 (18.30)	6.63 $\pm$ 0.17 (6.89)	1.63 $\pm$ 0.33 (1.82)	0.55 $\pm$ 0.035 (0.67)	0.56 $\pm$ 0.030 (0.96)	0.022 $\pm$ 0.024 (0)	0.21 $\pm$ 0.038 (0.18)
$\sigma$	56.85 $\pm$ 0.79 (52.70)	31.78 $\pm$ 0.48 (36.05)	2.01 $\pm$ 0.14 (2.12)	5.64 $\pm$ 0.27 (8.27)	0.95 $\pm$ 0.023 (0.35)	0.45 $\pm$ 0.035 (0.52)	0.064 $\pm$ 0.037 (0)	0.042 $\pm$ 0.031 (0)
$\chi$	52.04 $\pm$ 0.37 (55.80)	25.78 $\pm$ 0.36 (23.30)	2.05 $\pm$ 0.083 (2.22)	16.70 $\pm$ 0.68 (18.67)	1.22 $\pm$ 0.042 (0)	0.44 $\pm$ 0.032 (0)	0.355 $\pm$ 0.058 (0)	0.041 $\pm$ 0.037 (0)

**Table IV. Composition (Weight Percent) of CD3MWCuN Phases by WDS; the Equilibrium Phase Compositions Calculated by Thermo-Calc Using the TCFe3 Database are Shown in Parentheses (Our Calculations Show that the  $\delta$  Phase is Thermodynamically Unstable in CD3MWCuN at 850 °C)**

Phases	Fe	Cr	Ni	Mo	Si	Mn	W	Cu
(a) CD3MW/CuN Sample Annealed 10 Min at 850 °C								
$\delta$	58.52 $\pm$ 1.36	26.62 $\pm$ 0.60	5.66 $\pm$ 0.26	4.18 $\pm$ 0.43	0.85 $\pm$ 0.032	0.60 $\pm$ 0.033	0.70 $\pm$ 0.087	0.56 $\pm$ 0.065
$\gamma$	61.14 $\pm$ 0.34	23.40 $\pm$ 0.22	8.57 $\pm$ 0.096	2.65 $\pm$ 0.033	0.74 $\pm$ 0.020	0.70 $\pm$ 0.013	0.48 $\pm$ 0.036	0.74 $\pm$ 0.033
$\sigma$	55.92 $\pm$ 1.45	28.36 $\pm$ 1.29	5.06 $\pm$ 0.42	5.49 $\pm$ 0.99	0.94 $\pm$ 0.053	0.64 $\pm$ 0.039	0.91 $\pm$ 0.15	0.40 $\pm$ 0.10
$\chi$	no data obtained							
(b) CD3MW/CuN Sample Annealed 3 Days at 850 °C								
$\delta$	not present							
$\gamma$	61.43 $\pm$ 1.00(67.43)	22.65 $\pm$ 0.60 (18.26)	8.48 $\pm$ 0.55 (9.48)	2.31 $\pm$ 0.16 (1.84)	0.69 $\pm$ 0.043 (0.96)	0.68 $\pm$ 0.048 (0.73)	0.39 $\pm$ 0.036 (0.29)	0.88 $\pm$ 0.051 (0.95)
$\sigma$	54.36 $\pm$ 1.90 (50.12)	31.27 $\pm$ 1.23 (37.99)	3.73 $\pm$ 0.46 (2.42)	6.60 $\pm$ 1.41 (6.89)	1.09 $\pm$ 0.040 (0.76)	0.59 $\pm$ 0.071 (0.28)	1.18 $\pm$ 0.36 (1.53)	0.24 $\pm$ 0.072 (0)
$\chi$	50.85 $\pm$ 0.39 (51.26)	26.66 $\pm$ 0.46 (23.32)	2.78 $\pm$ 0.023 (2.85)	15.10 $\pm$ 0.83 (16.61)	1.17 $\pm$ 0.013 (0)	0.57 $\pm$ 0.0014 (0)	2.69 $\pm$ 0.19 (5.96)	0.15 $\pm$ 0.018 (0)

#### D. Precipitation Kinetics of $\sigma$ and $\chi$

The volume percentages of  $\sigma$  and  $\chi$  were determined by analysis of BSE images similar to that of Figure 5, and the results are shown in Figures 6 and 7 for CD3MN and CD3MWCuN, respectively. While it

appears that  $\chi$  may form initially in CD3MN, the amount remains extremely low when compared to  $\sigma$ . After 30 days annealing, the  $\chi$  phase in CD3MN had a maximum of about 2 vol pct at 800 °C and about 1 vol pct at 850 °C. At 900 °C, the amount of  $\chi$  phase was essentially zero. For CD3MWCuN, in which it appeared that  $\sigma$  formed first, the amount of  $\chi$  was also small, even less than seen for CD3MN. The maximum amount was about 1.5 vol pct at 800 °C. At 900 °C and 750 °C,  $\chi$  was not found after 3 days heat treatment. The kinetic curves for the extent of  $\sigma$  formation at a given temperature were found to be approximately sigmoidal in shape, which is in agreement with our previously reported results based on optical microscopy.<sup>[13]</sup>

The precipitation curves representing 1 vol pct formation of  $\sigma$  and  $\chi$  in CD3MN and CD3MWCuN are plotted in Figures 8 and 9, respectively. The 1 vol pct intermetallic phase precipitation curve ( $\sigma + \chi$ ) previously determined from optical microscopy study<sup>[13]</sup> is included for comparison. The noses of the  $\sigma$  and  $\chi$  curves match the previously reported curves fairly well, although the 1 vol pct  $\sigma$  curve is displaced to shorter times while  $\chi$  is displaced to longer times for CD3MN. The maximum formation temperature of  $\chi$  is located at approximately 900 °C, although the amount seen at this temperature never reached the 1 vol pct level for the times studied.

For CD3MWCuN, the noses for the  $\sigma$  and  $\chi$  phases were located at longer times than for the optically determined  $\sigma + \chi$  curve. The nose of the  $\chi$ -phase curve exists at a lower temperature than that for the  $\sigma$  phase. The temperature range for  $\chi$ -phase formation is between 750 °C and 900 °C.

#### IV. DISCUSSION

The phases identified from TEM analysis are in general agreement with what has been previously reported in DSS.<sup>[1]</sup> Although the  $M_7C_3$ , R, and  $\pi$  phases were not seen, this does not mean they were not present, as it is possible that the amounts of these phases were too low to be resolved in this study. If so, it is reasonable to conjecture that such irresolvable amounts of these secondary phases would play little or no role in determining the mechanical and corrosion properties of DSS and did not significantly affect the kinetics of microstructural evolution.

The measured phase compositions summarized in Tables III and IV, coupled with complementary microstructural analyses, indicate that  $\chi$  is most likely the first intermetallic phase to form in CD3MN. However, the composition of the initial precipitates is closer to that of  $\sigma$  than  $\chi$  in the case of CD3MWCuN. This may be due to the fact that, as shown in Figure 10, the thermodynamic driving forces for the precipitation of  $\sigma$  and  $\chi$  phases from metastable  $\gamma + \delta$  equilibrium are very similar to each other in both CD3MN and CD3MWCuN. As a consequence, a slight local composition fluctuation could easily affect which phase actually forms initially at any given location.

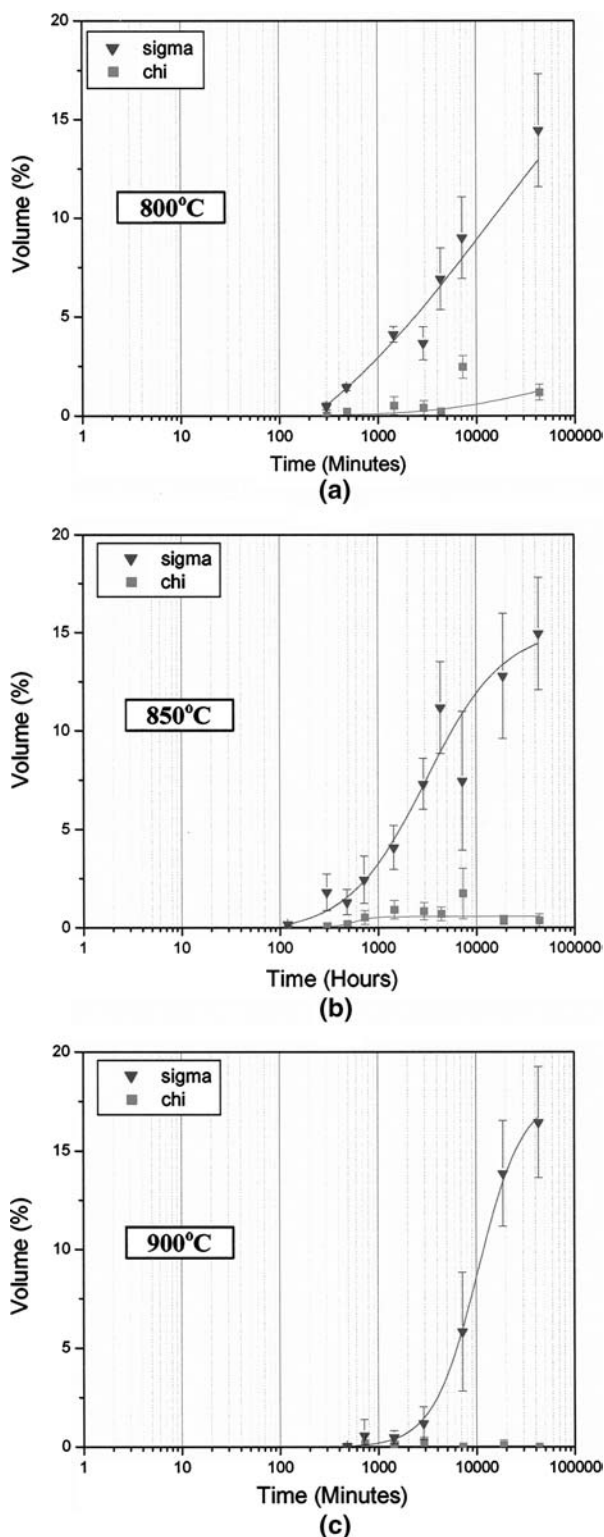


Fig. 6—Volume percent of  $\sigma$  and  $\chi$  at (a) 800 °C, (b) 850 °C, and (c) 900 °C.

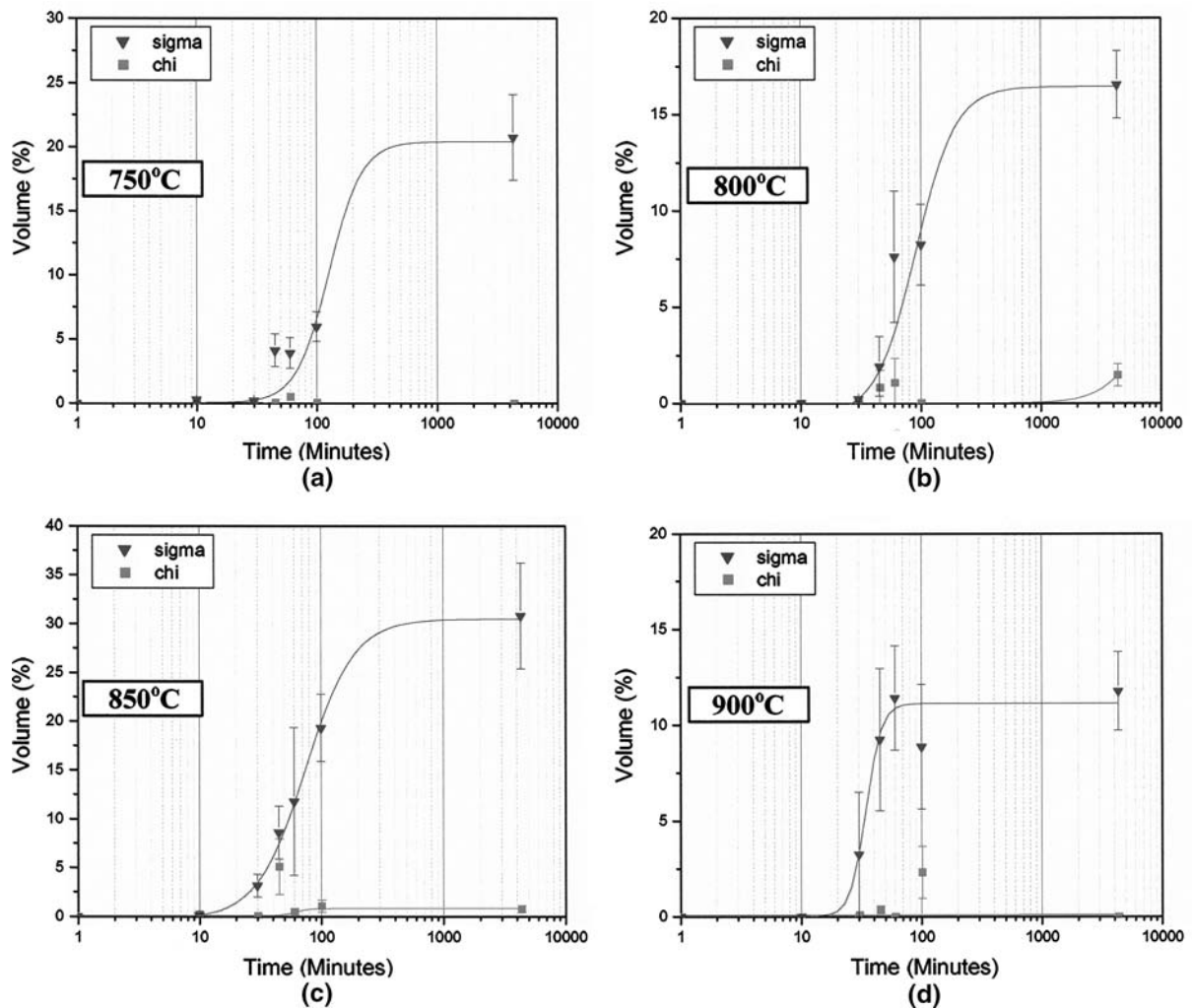


Fig. 7—Volume percent of  $\sigma$  and  $\chi$  at (a) 750 °C, (b) 800 °C, (c) 850 °C, and (d) 900 °C in CD3MWCuN.

In Figure 5, only limited amounts of  $\chi$  can be observed in contrast to the relatively high volume percentage of  $\sigma$ , and  $\chi$  precipitates usually appear inside

large  $\sigma$  regions. Indeed, the present equilibrium thermodynamic calculations do show that  $\sigma$  exists in much larger amounts than  $\chi$  in both CD3MN and

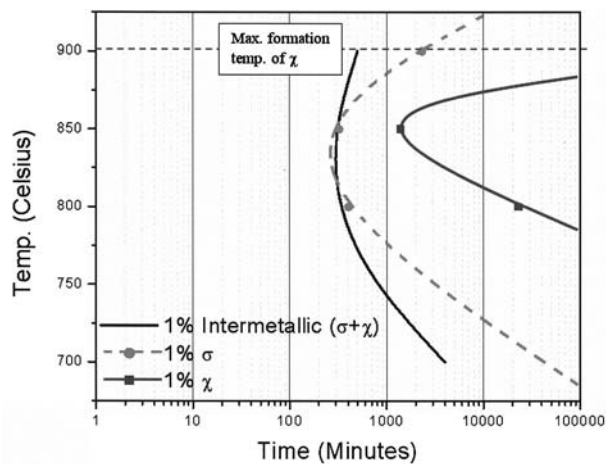


Fig. 8—Initial (1 vol pct) precipitation curves of  $\sigma$  and  $\chi$  phases superimposed on the initial intermetallic ( $\sigma + \chi$ ) curve after Ref. 13.

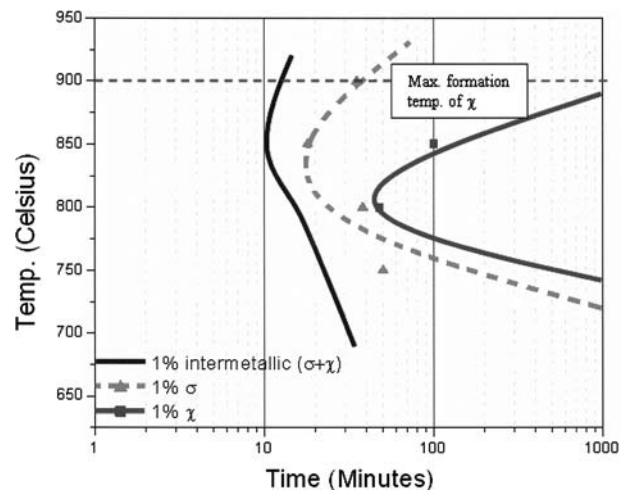


Fig. 9—Initial (1 vol pct) precipitation curves of  $\sigma$  and  $\chi$  phases for CD3MN superimposed on the TTT intermetallic ( $\sigma + \chi$ ) curve after Ref. 13.

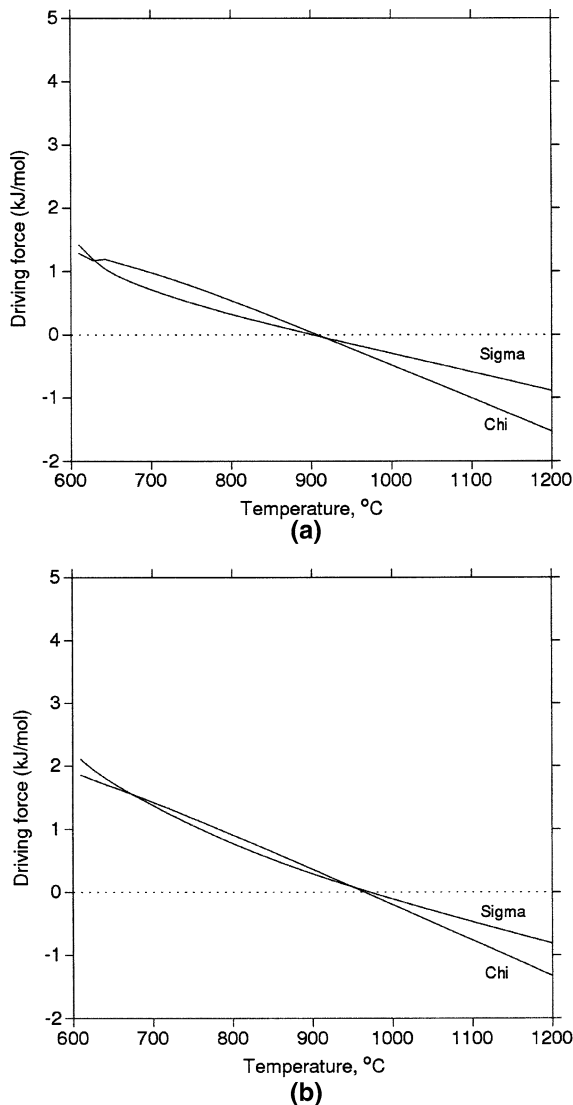


Fig. 10—Calculated thermodynamic driving force for the precipitation of  $\sigma$  and  $\chi$  phases from the metastable  $\sigma + \delta$  two-phase equilibrium as a function of temperature: (a) CD3MN and (b) CD3MWCuN.

CD3MWCuN at 850 °C. The extremely low amounts of  $\chi$  that formed make it difficult to reliably plot initial and final curves for this phase. The 1 vol pct curve was plotted to show the existence of such a phase. The temperature range for  $\chi$  precipitation was found between 750 °C and 900 °C, which is narrower than that found for the  $\sigma$  phase. The location of the nose was found to be similar to that seen for the same amount of  $\sigma$ , only slightly lower and delayed in time.

Finally, the discrepancy between the position of the precipitation start curve determined in an earlier study using optical microscopy<sup>[13]</sup> and the results of this study are believed to be primarily related to the techniques used and the number of samples examined. The SEM allowed for higher magnifications to be employed so small precipitates that may have been hard to distinguish using tint etching and an optical microscope were easily revealed in the SEM. This accounted for the

displacement of the initial precipitation curves to the left. In a similar manner, regions thought to be  $\sigma$  using optical means could be revealed as pits or inclusions using the higher resolution SEM. These possible variations, coupled with the minor variations that must be expected when examining different samples and areas, can easily account for the discrepancies.

## V. CONCLUSIONS

1. Phase identification in heat-treated CD3MN and CD3MWCuN DSS was carried out using SEM and TEM. The phases identified were  $\gamma$ ,  $\gamma_2$ ,  $\delta$ ,  $\sigma$ ,  $\chi$ ,  $\text{Cr}_{23}\text{C}_6$ , and  $\text{Cr}_2\text{N}$ .
2. The principal secondary phases to form in both steels were  $\sigma$  and  $\chi$ . At equilibrium, *i.e.*, after long-term annealing,  $\sigma$  is the predominant phase. Sigma is rich in Cr, approximately 31 wt pct, while  $\chi$  phase is rich in Mo, approximately 16 wt pct.
3. Resulting precipitation curves for  $\sigma$  and  $\chi$  showed slight variations between the results of this study and a previous one that employed optical microscopy for the quantitative analysis.<sup>[13]</sup> The maximum temperature for  $\chi$  formation is lower than that for  $\sigma$  formation.

## ACKNOWLEDGMENTS

This work was funded by the United States Department of Energy (USDOE) via a subcontract with the University of Alabama at Birmingham and was in collaboration with the Steel Founders' Society of America (SFSA) and their members. The TEM work was performed at Ames Laboratory under Contract No. W-7405-Eng-82 with the United States Department of Energy. The authors thank Alfred Kracher, Susan Shen, and Allison McNichols for assisting with this study.

## REFERENCES

1. *Special Report No. 31*, M. Blair, ed., Steel Founders' Society of America, 2001, pp. 1–52.
2. K.M. Lee, H.S. Cho, and D.C. Choi: *J. Alloys Compounds*, 1999, vol. 285, pp. 156–61.
3. A.J. Ramirez, J.C. Lippold, and S.D. Brandi: *Metall. Trans. A*, 2003, vol. 34A, pp. 1575–97.
4. Y.H. Lee, K.T. Kim, Y.D. Lee, and K.Y. Kim: *Mater. Sci. Technol.*, 1998, vol. 14, pp. 757–64.
5. S.-B. Kim, K.-W. Paik, and Y.-G. Kim: *Mater. Sci. Eng. A*, 1997, vol. 247, pp. 67–74.
6. *Duplex Stainless Steels: Microstructure, Properties and Applications*, R.N. Gunn, ed., Abington Publishing, 1997.
7. J.-O. Nilsson, P. Kangas, T. Karlsson, and Q. Wilson: *Metall. Trans. A*, 2000, vol. 31A, pp. 35–45.
8. *Proc. Conf. Duplex Stainless Steels '83*, R.A. Lula, ed., ASM, Metals Park, OH, 1983, vol. 1, pp. 693–756.
9. H.D. Solomon and T.M. Devine: *ASTM STP 672*, ASTM, Philadelphia, PA, 1979, pp. 430–61.



10. B. Josefsson, J.-O. Nilsson, and A. Wilson: in *Duplex Stainless Steels '91*, J. Charles and S. Bernhardsson, eds., Les Editions de Physique, Beaune, France, 1991, vol. 1, pp. 67–75.
11. X.G. Wang, D. Dumortier, and Y. Riquier: in *Duplex Stainless Steels '91*, J. Charles and S. Bernhardsson, eds., Les Editions de Physique, Beaune, France, 1991, vol. 1, pp. 127–34.
12. E. Johnson, Y.-J. Kim, L.S. Chumbley, and B. Gleeson: *Scripta Mater.*, 2004, vol. 50, pp. 1351–54.
13. Y.-J. Kim, L.S. Chumbley, and B. Gleeson: *Metall. Mater. Trans. A*, 2004, vol. 35A, pp. 3377–86.
14. M.E. Wilms, V.J. Gadgil, J.M. Krougman, and F.P. Ijsseling: *Corr. Sci.*, 1994, vol. 36, pp. 871–75.
15. J. Charles: *Proc. Conf. Duplex Stainless Steels '91*, Les Editions de Physique, Beaune, France, 1991, vol. 1, pp. 3–48.
16. J.-O. Nilsson, P. Kangas, T. Karlsson, and Q. Wilson: *Metall. Trans. A*, 2000, vol. 31A, pp. 35–45.
17. J.-O. Andersson, T. Helander, L. Hoglund, P.-F. Shi, and B. Sundman: *Calphad*, 2002, vol. 26, pp. 273–312.